Compensatory water effects link yearly global land CO₂ sink changes to temperature

Martin Jung[1], Markus Reichstein[1,2], Christopher R Schwalm[3], Chris Huntingford[4], Stephen Sitch[5], Anders Ahlström[6,7], Almut Arneth[8], Gustau Camps-Valls[9], Philippe Ciais[10], Pierre Friedlingstein[11], Fabian Gans[1], Kazuhito Ichii[12,13], Atul K. Jain[14], Etsushi Kato[15], Dario Papale[16], Ben Poulter[17], Botond Raduly[16,20], Christian Rödenbeck[18], Gianluca Tramontana[16], Nicolas Viovy[10], Ying-Ping Wang[19], Ulrich Weber[1], Sönke Zaehle[1,2], Ning Zeng[21]

[1]Max Planck Institute for Biogeochemistry, Department of Biogeochemical Integration, 07745 Jena, Germany

[2]Michael-Stifel-Center Jena for Data-driven and Simulation Science, 07743 Jena, Germany

[3]Woods Hole Research Center, 149 Woods Hole Rd, Falmouth, MA 02540, USA

[4]Centre for Ecology and Hydrology, Wallingford, Oxfordshire, OX10 8BB, U.K.

[5]College of Life and Environmental Sciences, University of Exeter, Exeter, UK.

[6]Department of Earth System Science, School of Earth, Energy and Environmental Sciences, Stanford University, Stanford, CA 94305, USA

[7]Lund University, Department of Physical Geography and Ecosystem Science, 223 62 Lund, Sweden.

[8]Karlsruhe Institute of Technology (KIT), Institute of Meteorology and Climate Research, 82467 Garmisch-Partenkirchen, Germany

[9]Image Processing Laboratory (IPL), C/ Catedrático José Beltran, 2. 46980 Paterna, València. Spain.

[10]Laboratoire des Sciences du Climat et de l'Environnement, CEA CNRS UVSQ, 91191 Gif-sur-Yvette, France

[11]College of Engineering, Mathematics and Physical Sciences, University of Exeter, Exeter, EX4 4QE, UK.

[12]Department of Environmental Geochemical Cycle Research, Japan Agency for Marine-Earth Science and Technology (JAMSTEC), 3173-25, Showa-machi, Kanazawa-ku, Yokohama, 236-0001, Japan

[13]Center for Global Environmental Research, National Institute for Environmental Studies, 16-2, Onogawa, Tsukuba, 305-8506, Japan

31 [14]Department of Atmospheric Sciences, University of Illinois,Urbana, IL 61801, USA

32 [15] Global Environment Programs, The Institute of Applied Energy (IAE), Tokyo, 105-0003, Japan

33 [16]Department for Innovation in Biological, Agro-food and Forest systems (DIBAF), Via San Camillo de

34 lellis snc, 01100 Viterbo, Italy.

35 [17]Department of Ecology, Montana State University, Bozeman, MT 59717

36 [18]Max Planck Institute for Biogeochemistry, Department of Biogeochemical Systems, 07745 Jena,

37 Germany

38 [19]CSIRO Ocean and Atmosphere, PMB #1, Aspendale, Victoria 3195, Australia

39 [20]Dept. of Bioengineering, Sapientia Hungarian University of Transylvania, 530104 M-Ciuc, Romania

40 [21]Dept. of Atmospheric and Oceanic Science, University of Maryland, College Park, MD 20742, USA

41

Large interannual variations in the measured growth rate of atmospheric carbon dioxide originate primarily from fluctuations in the carbon uptake by land ecosystems[1-3]. It remains uncertain, however, to what extent temperature and water availability control the carbon balance of land ecosystems across spatial and temporal scales[3-14]. Here we use eddy covariance data-derived empirical models[15] and process based models[16,17] to investigate the effect of changes in temperature and water availability on gross primary productivity (GPP), terrestrial ecosystem respiration (TER) and net ecosystem exchange (NEE) at local and global scales. We find that water availability is the predominant driver of the interannual variability in GPP, TER and, to a lesser extent, NEE at the local scale. When integrated globally, however, temporal NEE variability is mostly driven by temperature fluctuations ($R^2 \geq 0.84$). We suggest that this apparent paradox can be explained by two compensatory water effects. Temporal water driven GPP and TER variations compensate locally, dampening water-driven NEE variability. Spatial water availability anomalies also compensate, leaving a dominant temperature signal in the year-to-year fluctuations of the land carbon sink. These findings help reconcile seemingly contradictory reports regarding the importance of temperature and water in controlling the interannual variability of the terrestrial carbon balance[3-6,9,11,12,14]. Our study indicates that spatial climate co-variation drives the global carbon cycle response.

Large interannual variations in the recent measured atmospheric CO_2 growth rates originate primarily from fluctuations in carbon uptake by land ecosystems, rather than from oceans or variations in anthropogenic emissions[1-3]. There is a general consensus that the tropical region contributes the most to terrestrial carbon variability[1,8,18,19]. The observed positive correlation between mean tropical land temperature and CO_2 growth rate[3,5,6,12,13] implies smaller land carbon uptake and enhanced atmospheric CO_2 growth during warmer years with a sensitivity of about 5 GtC $yr^{-1}K^{-1}$. There is a tight relationship between this sensitivity on interannual time scales and long-term changes in terrestrial carbon per degree of warming across multiple climate carbon-cycle models[6]. Despite this strong emergent relationship with mean tropical land temperature, several studies suggest that variations in water availability play an important[8,10,11,14], even a dominant role[4,9], in shaping the interannual variability of the carbon balance of extensive semi-arid and sub-tropical systems. Furthermore, the recent doubling of the tropical carbon cycle sensitivity to interannual temperature variability has been linked to interactions with changing moisture regimes[13]. A full understanding of the processes governing the climatic controls of terrestrial carbon cycling on interannual time scales and across spatial scales is therefore still lacking. Here we show that the "temperature vs. water" debate can be resolved by simultaneously assessing the carbon cycle response to fluctuations in both temperature and water availability at both local and global scales.

Using both machine learning algorithms and process-based global land models, we derived spatial and temporal patterns of the interannual variability (IAV) of CO_2 uptake by plants via photosynthesis (gross primary production, GPP) and of CO_2 loss through respiration (terrestrial ecosystem respiration, TER). This allows analysis of net CO_2 ecosystem exchange (NEE=TER-GPP) IAV. Machine learning algorithms were used to translate gridded inputs of daily air temperature, water availability and radiation, among others[15], into time varying 0.5° grids of TER and GPP for the 1980-2013 period (FLUXCOM, see Methods). Three machine learning algorithms were trained on FLUXNET[20] based in situ TER and GPP flux estimates from two flux partitioning methods[21,22]. These three fitting algorithms combined with two partitioning methods provided six sets of GPP and TER estimates each, which combined yield 36 FLUXCOM NEE ensemble members. In a complementary approach,

86 we examined simulations of GPP and TER from an ensemble of seven global land surface or dynamic
87 vegetation models[16,17] (TRENDYv3, see Methods). These process-based model simulations follow a
88 common protocol and used the same climate forcing data set as the observation-based FLUXCOM
89 models. Both sets of results are expected to be more uncertain in the tropics due to less reliable
90 climate and satellite based inputs and a sparse coverage of flux measurements[23].

91 We analysed FLUXCOM and TRENDYv3 simulations independently, but in a consistent manner. We
92 derived NEE as the difference between TER and GPP, i.e., a positive value of NEE indicates a flux of
93 carbon from the land to the atmosphere. To isolate IAV we detrended GPP and TER for each grid cell
94 and month (see Methods). We find that global patterns of NEE interannual variability are consistent
95 between FLUXCOM and TRENDYv3 (EDF 1, SI-1). Both approaches reproduce (r ~ 0.8) the globally
96 integrated NEE IAV derived from atmospheric CO_2 concentration measurements and transport[24].
97 Both approaches also show the largest IAV in the tropics (EDF 1). To obtain the contributions of
98 different environmental variables to IAV, we decomposed carbon flux anomalies ($\Delta Flux$) of each year
99 (y), month (m), and grid cell (s) into their additive components forced by detrended anomalies of
100 temperature ($\Delta TEMP$), shortwave incoming radiation (ΔRAD), and soil-moisture related water
101 availability (ΔWAI, see Methods):

102 $$\Delta Flux_{s,m,y} = a_{s,m}^{TEMP} \times \Delta TEMP_{s,m,y} + a_{s,m}^{RAD} \times \Delta RAD_{s,m,y} + a_{s,m}^{WAI} \times \Delta WAI_{s,m,y} + \varepsilon_{s,m,y}$$

103 $$\Delta Flux_{s,m,y} \approx \Delta Flux_{s,m,y}^{TEMP} + \Delta Flux_{s,m,y}^{RAD} + \Delta Flux_{s,m,y}^{WAI} . \qquad \text{EQ (1)}$$

104 Here $a_{s,m}$ represents the estimated sensitivity of the flux anomaly, $\Delta Flux_{s,m,y}$ (GPP or TER) to each
105 respective climate forcing anomaly ($\Delta TEMP$, ΔRAD, ΔWAI) for a given grid cell and month, and $\varepsilon_{s,m,y}$
106 is the residual error term. The product of a given sensitivity (e.g. a^{TEMP}) and corresponding climate
107 forcing anomaly (e.g. $\Delta TEMP$) constitutes the flux anomaly component driven by this climate factor
108 (e.g. GPP^{TEMP}). Thus, Eq.1 estimates the contributions of temperature, radiation, and water
109 availability anomalies to carbon flux anomalies (see SI-2 for verification).

110 Our analysis reveals a contrasting pattern of NEE IAV controlled by temperature or moisture,
111 depending on spatial scale. At the global scale, temperature drives spatially-integrated NEE IAV (Fig.1
112 a,b, compare green and black curves), in line with previous findings based on correlations between
113 anomalies in temperature and CO_2 growth rate[3,5,6,12,13]. Globally integrated NEE anomalies due to
114 variations in radiation (NEE^{WAI}) and water availability (NEE^{WAI}) play only a minor role (compare blue
115 and black curves in Fig. 1a,b). The dominant global influence of temperature is in contrast to the
116 dominant local influence of water availability when analyzing all grid cells individually (Fig 1 c,d,
117 zonal mean of grid cell IAV; compare blue and black curves). Radiation causes the smallest NEE IAV at
118 grid cell level (red curve in Fig.1c,d) but there are indications based on other climate forcing data that
119 radiation could play a more important role than temperature locally (SI-3). Temperature variations
120 are important for NEE IAV (green curve in Fig.1c,d) in high latitudes and the inner tropics, but in
121 general, the grid cell average water related NEE variability (NEE^{WAI}, blue curve) is larger. Water
122 related NEE variability peaks at subtropical latitudes where semi-arid ecosystems dominate. This
123 finding is consistent with studies emphasizing the role of water limited semi-arid ecosystems on
124 global NEE IAV[4,9]. We now assess how this can be reconciled with the emergent temperature control
125 of globally integrated NEE IAV. Going from grid-cell to global scale shifts the emerging controls on
126 NEE IAV from water availability (local) towards temperature (global).

127   [Insert Figure 1 around here]

128   We hypothesized that the dominance of temperature in globally integrated NEE IAV results from a
129   stronger compensation of positive and negative NEE^{WAI} anomalies between different grid cells
130   compared to NEE^{TEMP} when going from local to global scale. To test this, we first illustrate the
131   dominant spatial patterns of temperature vs. water compensation using empirical orthogonal
132   functions (EOF) of the annual NEE^{TEMP} and NEE^{WAI} anomalies (Fig. 2 a-d). Here, the leading EOF of
133   NEE^{WAI} (~10% variance explained) has strong anti-correlated spatial patterns of positive and negative
134   values (Fig 2c,d), which correspond to ENSO imprints on moisture effects (R^2 with Nino 3.4 SST
135   index[25] of 0.75). In comparison, the leading EOF of NEE^{TEMP} (~22% variance explained) shows a more
136   spatially uniform response, and in particular across the tropics (Fig 2a,b). This pattern of much larger
137   spatial coherence of NEE^{TEMP} anomalies, compared to NEE^{WAI} anomalies, is also evident in their
138   respective sums of positive and negative covariances among all grid cells (inset pie charts in Fig 2. a-
139   d). For NEE^{TEMP} the sum of positive covariances is far larger than the negative ones (79% vs. 21%),
140   whereas positive and negative covariances are almost in balance (53% vs. 47%) for NEE^{WAI}. As a
141   consequence of the larger spatial coherence of NEE^{TEMP} anomalies, as compared to NEE^{WAI} anomalies,
142   we observe a shift of the dominant NEE IAV control from water at the local scale to temperature at
143   the global scale. We illustrate this change in Fig 2e,f by presenting relative dominance of water and
144   temperature related NEE IAV for increasing levels of spatial aggregation. This is a robust feature
145   within and among FLUXCOM and TRENDY approaches (EDF 2). We also find that the rise and decay of
146   NEE^{TEMP} and NEE^{WAI} dominance respectively with spatial scale occurs in all major biomes (SI-4). This
147   pattern is likely related to the different climatic characteristics of precipitation and air temperatures,
148   with the former, but not the latter, being associated with moisture conservation and offsetting
149   spatial anomaly patterns.

150   [Insert Figure 2 around here]

151   We now proceed to assess how local water and temperature related NEE IAV emerges from the
152   interaction of photosynthesis (GPP) and respiration (TER) processes. We compare the magnitudes of
153   water vs. temperature driven GPP and TER variability and find that WAI is overall the most important
154   factor controlling local IAV of both gross fluxes (Fig. 3 a-d), with particularly large variability in both
155   fluxes in semi-arid regions (SI-4, 5). However, the local IAV of NEE related to WAI (NEE^{WAI}, Fig. 3e, f) is
156   reduced compared to the components GPP^{WAI} and TER^{WAI}. Our results indicate that, in addition to the
157   spatial compensation of NEE^{WAI}, discussed above, there is also a local compensation mechanism,
158   whereby GPP^{WAI} and TER^{WAI} co-vary and thus locally counterbalance each other (Fig. 4 a, b). This is
159   likely due to the concomitant positive relationship of soil moisture with productivity and with
160   respiration. The combined effect is a smaller net effect of WAI on NEE. Specifically, two thirds of the
161   WAI effect on GPP is offset by the WAI effect on TER (0.67±0.33 for FLUXCOM, 0.69±0.14 for
162   TRENDY; mean slope ± s.d. across ensemble members of global TER^{WAI} vs. GPP^{WAI}). These patterns are
163   qualitatively consistent between the data-driven FLUXCOM (Fig. 4) and process-based TRENDY
164   models (EDF. 3) and agree with previous observations of simultaneous declines of GPP and TER[26-3025-
165   29] during droughts. However, magnitudes of TER^{WAI} vs. GPP^{WAI} covariances differ substantially among
166   model ensemble members (EDF 4). This likely reflects large uncertainty of respiration processes to
167   moisture variations while flux partitioning uncertainties seem negligible (SI-6).

168   [Insert Figure 3 around here]

169   In contrast to offsetting NEE water effects, our analysis indicates a weak local temperature

170   amplification effect of GPP and TER IAV in the tropics. Local temperature effects on GPP and TER IAV

171   are inversely correlated over the tropics (Fig. 4d). This is because GPP decreases with increasing

172   temperature, likely due to the exceedance of the thermal optimum of photosynthesis, whereas

173   respiration increases with temperature. Thus increasing temperatures in the tropics reduce NEE by

174   reducing GPP and increasing TER. However, due to lower variances of the temperature components

175   of GPP and TER (Fig. 3a-d), this local temperature amplification effect in the tropics is quantitatively

176   negligible (Fig. 4c) compared to the local water compensation effect (Fig. 4d). Overall, this causes the

177   difference of temperature vs. water forced variability of NEE to be smaller compared to the influence

178   of these drivers on the gross fluxes (compare distance between blue and green curves in Fig. 3 a-d vs.

179   e, f).

180   [Insert Figure 4 around here]

181   Our analysis shows water availability as the overall dominant driver of the interannual variability of

182   photosynthesis and respiration at local scales, even though this water signal is effectively absent in

183   the globally integrated NEE interannual variability. This pattern is driven by: 1) the local

184   compensatory effects of water availability on GPP and TER, and 2) the spatial anti-correlation of

185   water controlled NEE anomalies; and thus a compensation in space. These two compensatory water

186   effects leave temperature as the dominant factor globally, which resolves why there have been

187   conflicting conclusions surrounding whether NEE interannual variability is forced thermally or

188   hydrologically. Our analysis implies that climate does not only force the carbon cycle locally, but that,

189   perhaps more importantly, the spatial covariation of climate variables drives the integrated global

190   carbon cycle response. Consequently, any analysis conducted on integrated signals over larger

191   regions precludes inferences on the driving mechanisms at ecosystem scale. Likewise, the apparent

192   temperature dominated interannual variability of the residual land sink, a traditional target of global

193   carbon cycle modelers, contains little information on local carbon cycle processes. Our findings

194   suggest that potential changes in spatial covariations among climate variables associated with global

195   change may drive apparent changes of carbon cycle sensitivities and perhaps even the strength of

196   climate-carbon cycle feedbacks.

197

198   **References**

199

200   1   Bousquet, P. *et al.* Regional changes in carbon dioxide fluxes of land and oceans since 1980.
201   *Science* **290**, 1342-1346 (2000).

202   2   Keeling, C. D., Piper, S. C. & Heimann, M. in *Aspects of Climate Variability in the Pacific and*
203   *Western Americas* (ed D. H. Peterson) 305-363 (Washington, D.C., 1989).

204   3   Kindermann, J., Wurth, G., Kohlmaier, G. H. & Badeck, F. W. Interannual variation of carbon
205   exchange fluxes in terrestrial ecosystems. *Global Biogeochemical Cycles* **10**, 737-755,
206   doi:10.1029/96gb02349 (1996).

207   4   Ahlstrom, A. *et al.* The dominant role of semi-arid ecosystems in the trend and variability of
208   the land CO2 sink. *Science* **348**, 895-899, doi:10.1126/science.aaa1668 (2015).

209   5   Anderegg, W. R. L. *et al.* Tropical nighttime warming as a dominant driver of variability in the
210   terrestrial carbon sink. *Proceedings of the National Academy of Sciences* **112**, 15591-15596,
211   doi:10.1073/pnas.1521479112 (2015).

212　6　　Cox, P. M. *et al.* Sensitivity of tropical carbon to climate change constrained by carbon
213　　　dioxide variability. *Nature* **494**, 341-344, doi:10.1038/nature11882 (2013).
214　7　　Nemani, R. R. *et al.* Climate-driven increases in global terrestrial net primary production from
215　　　1982 to 1999. *Science* **300**, 1560-1563 (2003).
216　8　　Peylin, P. *et al.* Multiple constraints on regional CO2 flux variations over land and oceans.
217　　　*Global Biogeochemical Cycles* **19**, doi:10.1029/2003gb002214 (2005).
218　9　　Poulter, B. *et al.* Contribution of semi-arid ecosystems to interannual variability of the global
219　　　carbon cycle. *Nature* **509**, 600-603 (2014).
220　10　Tian, H. Q. *et al.* Effect of interannual climate variability on carbon storage in Amazonian
221　　　ecosystems. *Nature* **396**, 664-667, doi:10.1038/25328 (1998).
222　11　Wang, J., Zeng, N. & Wang, M. Interannual variability of the atmospheric CO2 growth rate:
223　　　roles of precipitation and temperature. *Biogeosciences* **13**, 2339-2352, doi:10.5194/bg-13-
224　　　2339-2016 (2016).
225　12　Wang, W. *et al.* Variations in atmospheric CO2 growth rates coupled with tropical
226　　　temperature. *Proceedings of the National Academy of Sciences of the United States of*
227　　　*America* **110**, 13061-13066, doi:10.1073/pnas.1219683110 (2013).
228　13　Wang, X. *et al.* A two-fold increase of carbon cycle sensitivity to tropical temperature
229　　　variations. *Nature* **506**, 212-215 (2014).
230　14　Zeng, N., Mariotti, A. & Wetzel, P. Terrestrial mechanisms of interannual CO(2) variability.
231　　　*Global Biogeochemical Cycles* **19**, doi:10.1029/2004gb0022763 (2005).
232　15　Tramontana, G. *et al.* Predicting carbon dioxide and energy fluxes across global FLUXNET
233　　　sites with regression algorithms. *Biogeosciences* **13**, 4291-4313, doi:10.5194/bg-13-4291-
234　　　2016 (2016).
235　16　Le Quéré, C. *et al.* Global carbon budget 2014. *Earth System Science Data Discussions* **7**, 521-
236　　　610 (2014).
237　17　Sitch, S. *et al.* Recent trends and drivers of regional sources and sinks of carbon dioxide.
238　　　*Biogeosciences* **12**, 653-679, doi:10.5194/bg-12-653-2015 (2015).
239　18　Gurney, K. R., Baker, D., Rayner, P. & Denning, S. Interannual variations in continental-scale
240　　　net carbon exchange and sensitivity to observing networks estimated from atmospheric
241　　　CO(2) inversions for the period 1980 to 2005. *Global Biogeochemical Cycles* **22**,
242　　　doi:Gb302510.1029/2007gb003082 (2008).
243　19　Peylin, P. *et al.* Global atmospheric carbon budget: results from an ensemble of atmospheric
244　　　CO2 inversions. *Biogeosciences* **10**, 6699-6720, doi:10.5194/bg-10-6699-2013 (2013).
245　20　Baldocchi, D. TURNER REVIEW No 15. 'Breathing' of the terrestrial biosphere: lessons learned
246　　　from a global network of carbon dioxide flux measurement systems. *Australian Journal of*
247　　　*Botany* **56**, 1-26 (2008).
248　21　Lasslop, G. *et al.* Separation of net ecosystem exchange into assimilation and respiration
249　　　using a light response curve approach: critical issues and global evaluation. *Global Change*
250　　　*Biology* **16**, 187-208 (2010).
251　22　Reichstein, M. *et al.* On the separation of net ecosystem exchange into assimilation and
252　　　ecosystem respiration: review and improved algorithm. *Global Change Biology* **11**, 1424-1439
253　　　(2005).
254　23　Schimel, D. *et al.* Observing terrestrial ecosystems and the carbon cycle from space. *Global*
255　　　*Change Biology* **21**, 1762-1776, doi:10.1111/gcb.12822 (2015).
256　24　Rödenbeck, C., Houweling, S., Gloor, M. & Heimann, M. CO2 flux history 1982–2001 inferred
257　　　from atmospheric data using a global inversion of atmospheric transport. *Atmos. Chem. Phys.*
258　　　**3**, 1919-1964, doi:10.5194/acp-3-1919-2003 (2003).
259　25　Rayner, N. A. *et al.* Global analyses of sea surface temperature, sea ice, and night marine air
260　　　temperature since the late nineteenth century. *Journal of Geophysical Research-*
261　　　*Atmospheres* **108**, doi:10.1029/2002jd002670 (2003).

262 26 Biederman, J. A. *et al.* Terrestrial carbon balance in a drier world: the effects of water
263   availability in southwestern North America. *Global Change Biology* **22**, 1867-1879,
264   doi:10.1111/gcb.13222 (2016).
265 27 Bonal, D., Burban, B., Stahl, C., Wagner, F. & Hérault, B. The response of tropical rainforests
266   to drought—lessons from recent research and future prospects. *Annals of Forest Science* **73**,
267   27-44, doi:10.1007/s13595-015-0522-5 (2016).
268 28 Ciais, P. *et al.* Europe-wide reduction in primary productivity caused by the heat and drought
269   in 2003. *Nature* **437**, 529-533 (2005).
270 29 Schwalm, C. R. *et al.* Assimilation exceeds respiration sensitivity to drought: A FLUXNET
271   synthesis. *Global Change Biology* **16**, 657-670 (2010).
272 30 van der Molen, M. K. *et al.* Drought and ecosystem carbon cycling. *Agricultural and Forest
273   Meteorology* **151**, 765-773 (2011).
274

293 **Author Contributions**
294 MJ and MR designed the analysis. MJ carried out the analysis and wrote the manuscript with
295 contributions from all authors. MJ, CRS, GCV, FG, KI, DP, BR, GT, and UW contributed to FLUXCOM
296 results. SS, PF, CH, AAl,Aar, PC, AKJ, EK, BP, NV, YPW, and NZ contributed to TRENDY results.

297 **Author Information**

298 Reprints and permissions information is available at http://www.nature.com/reprints. The authors
299 declare no competing financial interests. Correspondence and requests for materials should be
300 addressed to mjung@bgc-jena.mpg.de.

301
302

Figure captions

Figure 1: Climatic controls on NEE IAV at global and local scales for the period 1980-2013 derived from machine learning based (FLUXCOM) and process-based (TRENDY) models. *The comparison of globally integrated annual NEE anomalies with NEE anomalies driven only by temperature, water availability, and radiation (**a, b**) shows temperature as dominant global control. R^2 values between the climatic NEE components and total NEE are given in the respective colour. Mean grid cell IAV magnitude (see Equation 3 in Methods) in panels (**c**) and (**d**) of NEE components for latitudinal bands shows water as dominant local control. Uncertainty bounds where given as shaded area reflect the spread among FLUXCOM or TRENDY ensemble members (±1 s.d.).*

Figure 2: Effects of spatial co-variation and scale on temperature vs. water control of NEE IAV for FLUXCOM and TRENDY models. *Spatial patterns of the first empirical orthogonal function of annual NEE^{TEMP} (**a, b**), and NEE^{WAI} (**c, d**) anomalies (see Methods) show large spatial coherence for NEE^{TEMP} (dominant positive values) and anti-correlated patterns for NEE^{WAI} (positive and negative values; magnitudes are not informative and were omitted for clarity). This is underpinned in the inset pie charts which show the proportion of total positive (black) and negative (gray) co-variances among grid cells for NEE^{TEMP} and NEE^{WAI} anomalies (see Equation 4 and 5 in Methods). Panels **e, f** present how the relative dominance (see Equation 6 in Methods) of NEE^{TEMP} (green) increases with successive spatial aggregation, while the relative dominance of NEE^{WAI} (blue) decreases. Outer uncertainty bounds in **e,f**, given as shaded area refer to the spread among respective ensemble members (±1 s.d.); inner uncertainty bounds refer to ±1 s.d. with respect to the change of relative dominance with spatial aggregation (see Equation 7 in Methods).*

Figure 3: Latitudinal patterns of water and temperature driven IAV of gross carbon fluxes (GPP and TER) and NEE for FLUXCOM and TRENDY models. *IAV magnitude (see Equation 3 in Methods) of the WAI component is much larger than the IAV of the TEMP component for gross fluxes (a-d), while this difference is smaller for NEE due to compensation. Uncertainty bounds as shaded area reflect the spread among FLUXCOM or TRENDY ensemble members (±1 s.d.).*

Figure 4: Spatial patterns of covariance and correlation of WAI and TEMP driven GPP and TER IAV for FLUXCOM models. *Maps of the covariance of annual anomalies (see Equation 8 in Methods) of GPP and TER climatic components show large compensation effects (positive covariance) for WAI (**a**) but nearly no covariance for TEMP (**c**). Correlations between GPP^{WAI} and TER^{WAI} are large and ubiquitous positive (**b**) while correlations among GPP^{TEMP} and TER^{TEMP} are weaker with a distinct spatial pattern of negative correlations in hot regions (**d**). All results refer to the mean of all FLUXCOM ensemble members. See EDF 3 for equivalent TRENDY results, and EDF 4 for uncertainties.*

9

Methods

Global carbon flux data sets

FLUXCOM. Three machine learning methods were trained on daily carbon flux estimates from 224 flux tower sites using meteorological measurements and satellite data as inputs[15]: Random Forests[31], Artificial Neural Networks[32], Multivariate Adaptive Regression Splines[33]. Models were trained separately for two variants of GPP and TER, derived from the flux partitioning methods of Reichstein et al.[22] and Lasslop et al.[21]. Each method used the same 11 input driver data listed in Table SI-7. This set of driver data was obtained from an extensive variable selection analysis[15,34]. Details along with extensive model evaluation based on cross-validation are given in Tramontana et al.[15].

To produce spatio-temporal grids of carbon fluxes, the trained machine learning algorithms require only spatio-temporal grids of its input driver data[35]. We forced the models with grids of 0.5° spatial resolution and daily time step for the period 1980-2013[36]. High-resolution satellite based predictor variables (see Table SI-7) were tiled by plant functional type (PFT), i.e. grids for each PFT containing the mean value per PFT and time step at 0.5° were created. The PFT distribution originates from the majority class of annually resolved MODIS land cover product (collection 5)[37] for each high-resolution pixel. Climatic predictor variables are based on CRUNCEPv6 (http://esgf.extra.cea.fr/thredds/catalog/store/p529viov/cruncep/V6_1901_2014/catalog.html) to be consistent with the TRENDY ensemble. CRUNCEPv6 is based on a merged product of Climate Research Unit (CRU) observation based monthly 0.5° climate variables[38] (1901 – 2013) and the high temporal (6-hourly) resolution NCEP reanalysis. The variables affected by the climate forcing data set are marked in Table SI-7. Among the 11 predictor variables, only temperature, radiation, and water availability can generate interannual variability. The water availability index (WAI, see supplement 3 in Tramontana et al. [15]) is based on a simple dynamic soil water balance model, which was driven with daily precipitation and potential evapotranspiration by CRUNCEPv6 (see SI-8 for cross-consistency with TRENDY based soil moisture). The machine learning models were run at for each plant functional type (PFT) separately, and a weighted mean over the PFT fractions was obtained for each grid-cell. The PFT distribution is representative of the period 2001-2012; no land cover change was considered. Empirical models were run to spatially estimate GPP and TER. Then NEE was derived by the carbon mass balance approach (NEE = TER-GPP), which allows for decomposing precisely of how NEE IAV emerges from (co-)variations of TER and GPP. We verify that NEE IAV derived as TER-GPP is consistent with upscaling NEE directly (SI-6). Overall 36 combinations of NEE were derived by considering all possible combinations of TER-GPP realizations resulting from different machine learning approaches, and flux partitioning variants. The individual model runs were finally aggregated to monthly means.

TRENDY. We used simulations of seven Dynamic Global Vegetation Models (DGVMs) from the TRENDY v3 ensemble[16,17] for the period 1980-2013, which have a spatial resolution of 0.5° (model simulations with coarser resolution were omitted): CABLE[39], ISAM[40], LPJ[41], LPJ-GUESS[42], ORCHIDEE[43], VEGAS[14], VISIT[44]. These models were forced by a common set of input datasets and experimental protocol (experiment 'S2')[16,17]. Climate forcing (CRUNCEPv6) is the same as for FLUXCOM. Global atmospheric CO_2 was derived from ice core and NOAA monitoring station data, and provided at annual resolution over the period 1860-2013[16]. DGVMs were run from preindustrial steady state (NEE = 0) with changing fields of climate and atmospheric CO_2 concentration over the 20thC. Land Use and Land cover changes were not considered. For consistency with FLUXCOM, NEE was derived

381 as the difference between terrestrial ecosystem respiration (TER) and GPP, i.e. fire emissions
382 available from some models were not included. Terrestrial ecosystem respiration was calculated as
383 the sum of simulated autotrophic and heterotrophic respiration.
384

385 **Analysis**

386 **Anomalies and decomposition.** Detrended monthly anomalies were obtained by removing the linear
387 trend over years for each pixel and month (least squares fitting), which also centers the mean to zero
388 for a given pixel and month. This procedure was applied consistently to GPP, and TER, shortwave
389 radiation (RAD), air temperature (TEMP), and water availability (WAI), FLUXCOM and TRENDY
390 simulations. For TRENDY models the simulated soil moisture was used instead of WAI. The resulting
391 IAV of GPP and TER was decomposed into the contributions forced by TEMP, RAD, and WAI following
392 Eq.1 using a multiple linear (ordinary least squares) regression with zero intercept for each pixel and
393 month. NEE sensitivities and NEE components were derived from GPP and TER results, which is
394 equivalent to decomposing NEE (=TER-GPP) directly. We validate and discuss the approximation of
395 IAV contributions by Eq.1 in SI-2.

396 **Notations.** All analysis is based on detrended monthly anomalies (Eq. 1) aggregated to annual means.
397 For simplicity, we omit the Δ notation for 'anomaly' in the following. Superscripts 'TEMP', 'WAI',
398 'RAD' refer to surface air temperature, water availability, and incoming shortwave radiation of a
399 respective carbon flux anomaly. Subscripts 's','y','e' refer to indexes of grid cell, year, and ensemble
400 member respectively. The mean and standard deviation are denoted as μ and σ respectively, where
401 the subscripts of these operators tell whether the operation is done over grid cells (e.g. μ_s is an
402 average over all grid cells), years (e.g. σ_y is the standard deviation over the years), or ensemble
403 members. All main results refer to the mean of FLUXCOM or TRENDY ensemble members (μ_e) and
404 the standard deviation (σ_e) is used as uncertainty estimate. Whenever we calculated a mean over
405 0.5° grid cells (μ_s) we accounted for different grid cell areas (area weighted mean) and used a
406 consistent mask of valid values between FLUXCOM and TRENDY. Because several analyses are
407 referenced with respect to the sum of climatic components of NEE we denote NEE*:

408 $$NEE^*_{s,y} = NEE^{TEMP}_{s,y} + NEE^{WAI}_{s,y} + NEE^{RAD}_{s,y}$$ EQ (2)

409 **Spatial patterns of IAV magnitude (e.g. Fig. 1c,d & 3).** To describe spatial patterns of IAV magnitude
410 (M) of climatic components of carbon fluxes (e.g. GPP^{WAI}) we computed the standard deviation of its
411 annual values (σ_y) for each grid cell (s). This standard deviation was then normalized by the mean (μ_s)
412 temporal standard deviation (σ_y) of NEE* to provide a relative metric of IAV magnitude, where values
413 above 1 indicate IAV magnitudes larger than average NEE* IAV. This scaling accounts for the known
414 underestimation of IAV magnitude in the upscaling approach[35] but does not change any patterns.

415

416 $$M_s = \frac{\sigma_y(Flux^{COMP}_{s,y})}{\mu_s(\sigma_y(NEE^*_{s,y}))}$$ EQ (3)

417 Fig. 1c,d shows mean and standard deviations across ensemble members (μ_e and σ_e) for NEE
418 components for latitudinal bins of 5°. The same holds for Fig.3 which shows also GPP and TER
419 components.

420 **Empirical orthogonal functions and spatial covariances (Fig. 2a-d).** We first calculated mean spatio-
421 temporal grids of NEE climatic components across ensemble members ($\mu_e(NEE_{s,y,e}^{COMP})$). We then
422 multiplied those with grid cell areas to convert flux densities into fluxes per grid cell, and normalized
423 them by the standard deviation of NEE* across time and space ($\sigma_{s,y}(\mu_e(NEE_{s,y,e}^*))$). Empirical
424 orthogonal functions were then computed for each climatic component without additional scaling in
425 MATLAB using the 'pca' function. The spatial pattern of first principle components (leading EOFs) of
426 NEE^{TEMP} and NEE^{WAI} was plotted with the same color scale. The values on the color bar themselves
427 are not informative and were therefore omitted for clarity. The leading EOF explains about 22% of
428 spatial NEE^{TEMP} variance and ~10% of spatial NEE^{WAI} variance in both FLUXCOM and TRENDY
429 ensemble means.

430 To quantify the degree of spatial covariance of NEE climatic components (inset pie charts in Fig. 2a-d)
431 we calculated a large covariance matrix of all grid cells vs all grid cells for each NEE climatic
432 component (annual anomalies multiplied with grid cell area), where the elements of this covariance
433 matrix ($c_{i,j}^{COMP}$) were calculated according to Equation (4):

434 $$c_{i,j}^{COMP} = cov_y(NEE_{si,y}^{COMP}, NEE_{sj,y}^{COMP}) \hspace{3cm} \text{EQ (4)}$$

435 Here i and j index the two grid cells for which the covariance is calculated. By definition the variance
436 of the globally integrated anomalies equals the sum of all terms in the covariance matrix. To
437 determine the share of positive vs negative spatial covariance of the total variance, we summed
438 positive and negative covariance terms respectively (Equation 5). The sum of variances (the diagonal
439 of the covariance matrix where i=j) was omitted in the pie charts because they accounted for less
440 than 1% of the covariance budget.

441 $$tcov_+^{COMP} = \sum_{i=1}\sum_{j\neq i} c_{i,j}^{COMP} \mid c_{i,j}^{COMP} > 0; \; tcov_-^{COMP} = \sum_{i=1}\sum_{j\neq i} c_{i,j}^{COMP} \mid c_{i,j}^{COMP} < 0 \hspace{1cm} \text{EQ (5)}$$

442 **Scale dependence of relative dominance of NEE^{TEMP} and NEE^{WAI} (Fig. 2e,f).** We defined relative
443 dominance (D) of a climatic component (COMP) of NEE (e.g. NEE^{TEMP}) as the mean (μ_s) variance of
444 annual anomalies (σ_y^2) of this component divided by the mean variance of NEE*:

445 $$D^{COMP} = \frac{\mu_s(\sigma_y^2(NEE_{s,y}^{COMP}))}{\mu_s(\sigma_y^2(NEE_{s,y}^*))} \hspace{3cm} \text{EQ (6)}$$

446 To illustrate how this relative dominance changes systematically with spatial scale we aggregated
447 NEE components successively to coarser spatial resolutions starting at 0.5° (~54.000 grid cells) and
448 ending with 'global'(1 grid cell at 360 degrees resolution) and recomputed relative dominance for
449 each spatial resolution. In total 25 levels of spatial resolution were used: 0.5, 1, 1.5, 2.5, 3, 4, 4.5, 5,
450 6, 7.5, 9, 10, 12, 15, 18, 20, 22.5, 30, 36, 45, 60, 90, 180, 360 degrees.

451 These computations were carried out for each ensemble member separately and the mean across
452 ensemble members (μ_e) was plotted for each spatial resolution as dots connected with a line. The
453 uncertainty reflected by the spread of ensemble members (σ_e) was plotted as light shaded area. This
454 uncertainty is dominated by uncertainty of the mean relative dominance and not by uncertainty on
455 the systematic change with spatial aggregation. To visualize that we provided a dark shaded area in
456 the plots which represent the uncertainty on the 'shape of the curve' (U in Equation 7). This is based
457 on the standard deviation across ensemble members after subtracting the mean relative dominance
458 over all spatial resolutions (I in Equation 7) for each ensemble member (Equation 7). While Fig.2e,f

459 shows the effect of shifting relative dominance of NEE^{WAI} vs NEE^{TEMP} with spatial resolution

460 considering the entire global vegetated area, we repeated this analysis for different biomes (see SI-4)

461 by considering only grid cells belonging to a specific biome.

462 $$U_l = \sigma_e(D_{l,e} - \mu_l(D_{l,e}))$$ EQ (7)

463 **Covariance of temperature and water availability components of GPP and TER (Fig.4).** We

464 computed the correlation coefficient and covariance between GPP and TER components (e.g. GPP^{TEMP}

465 vs. TER^{TEMP}) for each grid cell and ensemble member. The covariance terms were normalized to the

466 mean variance of NEE* (Equation 8). Fig. 4 shows the mean across the ensemble members (μ_e) for

467 FLUXCOM, and EDF 3 the mean for the TRENDY ensemble. EDF 4 shows latitudinal patterns of the

468 spread among ensemble members (σ_e) for FLUXCOM and TRENDY. The robustness of FLUXCOM

469 results with respect to different NEE flux partitioning methods is assessed in SI-6.

470 $$normalized\ COV_s\left(GPP_{s,y}^{COMP}, TER_{s,y}^{COMP}\right) = \frac{COV_y\left(GPP_{s,y}^{COMP}, TER_{s,y}^{COMP}\right)}{\mu_s(\sigma_y^2(NEE_{s,y}^*))}$$ EQ (8)

471 **Comparison with atmospherically based data (EDF 1).** We used three data sources of

472 atmospherically based net CO_2 flux exchange. The first is based on the annually resolved Global

473 Carbon Budget (GCP) [13], which uses measurements of atmospheric CO_2 growth rate and estimates of

474 fossil fuel emissions, ocean uptake, and land use change emissions to derive the global land flux as a

475 residual. The second is based on the Jena CarboScope atmospheric transport inversion[24] (Jena

476 Inversion, version s81_3.7) covering the full time period of the study. The third is an ensemble of 10

477 atmospheric inversions[19] used for the REgional Carbon Cycle Assessment and Processes (RECCAP)

478 activity covering the period 1990-2012, with each inversion covering a different time period. Four

479 versions of the Jena Inversion have been removed from the original 14 member RECCAP ensemble to

480 make it an independent assessment. We used globally integrated net land CO_2 flux estimates from

481 the three data sources to assess globally integrated NEE IAV of FLUXCOM and TRENDY. For the Jena

482 and RECCAP inversions, we additionally calculated the integrated net land CO_2 flux for areas north

483 and south of 30°N. All time series were detrended. For RECCAP inversions we calculated the median

484 estimate of the available inversion estimates per year. All time series were normalized by the

485 standard deviation of the respective globally integrated annual net land CO_2 flux.

486 **References**

488 31 Breiman, L. Random forests. *Machine Learning* **45**, 5-32, doi:10.1023/a:1010933404324
489   (2001).

490 32 Haykin, S. *Neural Networks: A Comprehensive Foundation*. (Prentice Hall PTR, 1998).

491 33 Friedman, J. H. Multivariate Adaptive Regression Splines. *Annals of Statistics* **19**, 1-67,
492   doi:10.1214/aos/1176347963 (1991).

493 34 Jung, M. & Zscheischler, J. A guided hybrid genetic algorithm for feature selection with
494   expensive cost functions. *Procedia Computer Science* **18**, 2337-2346 (2013).

495 35 Jung, M. *et al.* Global patterns of land-atmosphere fluxes of carbon dioxide, latent heat, and
496   sensible heat derived from eddy covariance, satellite, and meteorological observations.
497   *Journal of Geophysical Research - Biogeosciences* **116**, G00J07, doi:10.1029/2010JG001566
498   (2011).

499 36 Jung, M. & FLUXCOM team FLUXCOM (RS+METEO) Global Land Carbon Fluxes using
500   CRUNCEP climate data. *FLUXCOM Data Portal*
501   http://dx.doi.org/10.17871/FLUXCOM_RS_METEO_CRUNCEPv6_1980_2013_v1 (2016)

502   37   Friedl, M. A. *et al.* MODIS Collection 5 global land cover: Algorithm refinements and
503   characterization of new datasets. *Remote Sensing of Environment* **114**, 168-182,
504   doi:http://dx.doi.org/10.1016/j.rse.2009.08.016 (2010).
505   38   New, M., Hulme, M. & Jones, P. Representing twentieth-century space-time climate
506   variability. Part II: Development of 1901-96 monthly grids of terrestrial surface climate.
507   *Journal of Climate* **13**, 2217-2238, doi:10.1175/1520-0442(2000)013<2217:rtcstc>2.0.co;2
508   (2000).
509   39   Wang, Y. P., Law, R. M. & Pak, B. A global model of carbon, nitrogen and phosphorus cycles
510   for the terrestrial biosphere. *Biogeosciences* **7**, 2261-2282, doi:10.5194/bg-7-2261-2010
511   (2010).
512   40   Jain, A. K., Meiyappan, P., Song, Y. & House, J. I. CO2 emissions from land-use change
513   affected more by nitrogen cycle, than by the choice of land-cover data. *Global Change*
514   *Biology* **19**, 2893-2906, doi:10.1111/gcb.12207 (2013).
515   41   Sitch, S. *et al.* Evaluation of ecosystem dynamics, plant geography and terrestrial carbon
516   cycling in the LPJ dynamic global vegetation model. *Global Change Biology* **9**, 161-185 (2003).
517   42   Smith, B., Prentice, I. C. & Sykes, M. T. Representation of vegetation dynamics in the
518   modelling of terrestrial ecosystems: comparing two contrasting approaches within European
519   climate space. *Global Ecology and Biogeography* **10**, 621-637, doi:10.1046/j.1466-
520   822X.2001.t01-1-00256.x (2001).
521   43   Krinner, G. *et al.* A dynamic global vegetation model for studies of the coupled atmosphere-
522   biosphere system. *Global Biogeochemical Cycles* **19**, GB1015, doi:1010.1029/2003GB002199
523   (2005).
524   44   Kato, E., Kinoshita, T., Ito, A., Kawamiya, M. & Yamagata, Y. Evaluation of spatially explicit
525   emission scenario of land-use change and biomass burning using a process-based
526   biogeochemical model. *Journal of Land Use Science* **8**, 104-122,
527   doi:10.1080/1747423X.2011.628705 (2013).
528

529   **Data availability.** The FLUXCOM data that support the findings of this study are available from the
530   Data Portal of the Max Planck Institute for Biogeochemistry (https://www.bgc-
531   jena.mpg.de/geodb/projects/Home.php) with the identifier
532   doi:10.17871/FLUXCOM_RS_METEO_CRUNCEPv6_1980_2013_v1. The TRENDY v3 data that support
533   the findings of this study are available from Stephen Sitch (S.A.Sitch@exeter.ac.uk) upon reasonable
534   request. Source data of Fig.1 a-d, Fig, 2 e-f, and Fig. 3 a-f are additionally provided as Excel
535   spreadsheets with the paper.

536

537   **Extended Data Figure Legends**

538   **Extended Data Figure 1: Global patterns of NEE IAV for FLUXCOM (left) and TRENDY (right)**. *Maps*
539   *of NEE IAV magnitude (mean of ensemble members, a, b) defined as standard deviation of annual*
540   *NEE normalized by the mean standard deviation (values above 1 indicate above average IAV). Dashed*
541   *lines separate areas north and south of 30°N. Time series of integrated NEE over broad latitudinal*
542   *bands (c-f) or global (g,h) for 1980-2013 normalized by the standard deviation of globally integrated*
543   *NEE. Black lines show the mean of FLUXCOM or TRENDY ensemble members and the shaded area*
544   *refers to the ensemble spread (1 s.d.). Independent estimates from the Global Carbon Project (GCP),*
545   *the Jena Inversion, and the Regional Carbon Cycle Assessment and Processes (RECCAP) inversions (see*
546   *Methods) are presented with coloured lines (see legend); correlation coefficients with those are given*
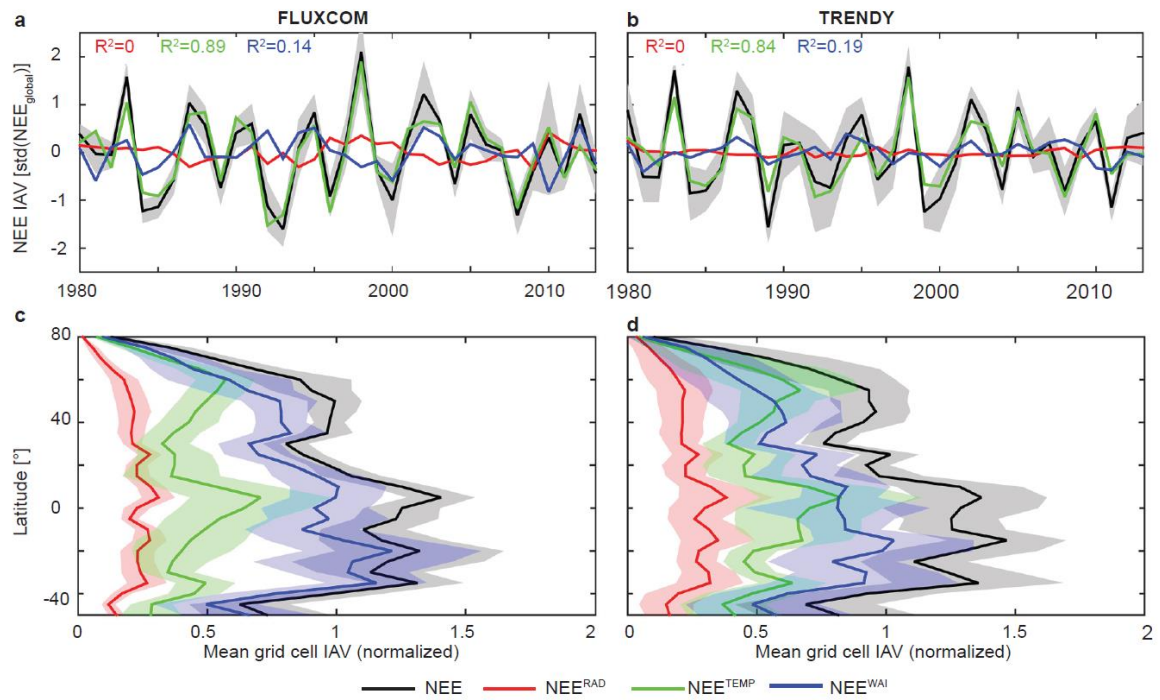547   *in the same colour. See SI-1 for further cross-consistency analysis.*

Extended Data Figure 2: Local vs global dominance of NEE^{TEMP} vs NEE^{WAI} for FLUXCOM and TRENDY ensemble members. *Dots show individual ensemble members and the crosses show ensemble means with one standard deviation. Plotted is the difference of local NEE^{WAI} and NEE^{TEMP} dominance (difference of blue and green most left data point in Fig.2 e,f, in main article) against the difference of global NEE^{WAI} and NEE^{TEMP} dominance (difference of blue and green most right data point in Fig.2 e,f, in main article). The majority of ensemble members as well as ensemble means fall in the lower right quadrant meaning an overall agreement that NEE^{WAI} dominates at individual grid cells ('locally') but NEE^{TEMP} the globally integrated flux anomaly ('global').*

Extended Data Figure 3: **Spatial patterns of covariance and correlation of WAI and TEMP driven GPP and TER IAV for TRENDY models.** *Maps of the covariance of annual anomalies (see Equation 8 in Methods) of GPP and TER climatic components show large compensation effects (positive covariance) for WAI (**a**) but nearly no covariance for TEMP (**c**). Correlations between GPP^{WAI} and TER^{WAI} are large and ubiquitous positive (**b**) while correlations among GPP^{TEMP} and TER^{TEMP} are weaker with a distinct spatial pattern of negative correlations in hot regions (**d**). All results refer to the mean of all FLUXCOM ensemble members. See Fig.4 for equivalent FLUXCOM results, and EDF 4 for uncertainties.*

Extended Data Figure 4: Ensemble spread of covariation between TEMP and WAI components of GPP and TER for FLUXCOM and TRENDY. *Plots show mean covariance (left) and correlation (right) between GPP^{TEMP} and TER^{TEMP} and GPP^{WAI} and TER^{WAI} for latitudinal bins of 5° for individual ensemble members (thin dotted lines) and ensemble mean (thick solid line with shaded area for 1 s.d.). Despite uncertain magnitudes of GPP^{TEMP} and TER^{TEMP} correlation (large green shaded area in right panels) their covariance is negligible (small shaded green area in left panels). In comparison, there is large positive covariance of GPP^{WAI} and TER^{WAI} but its magnitude differs substantially among ensemble members (large blue shaded area in left panels).*
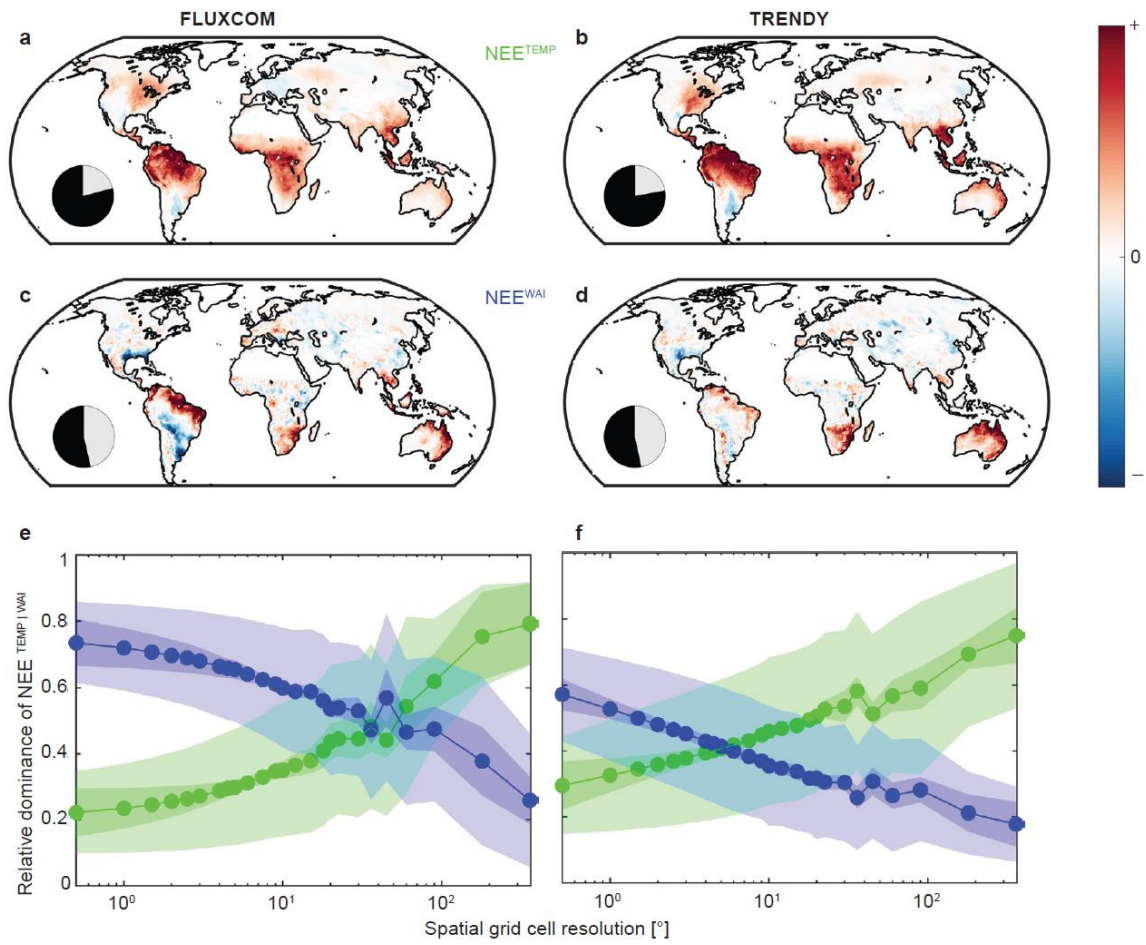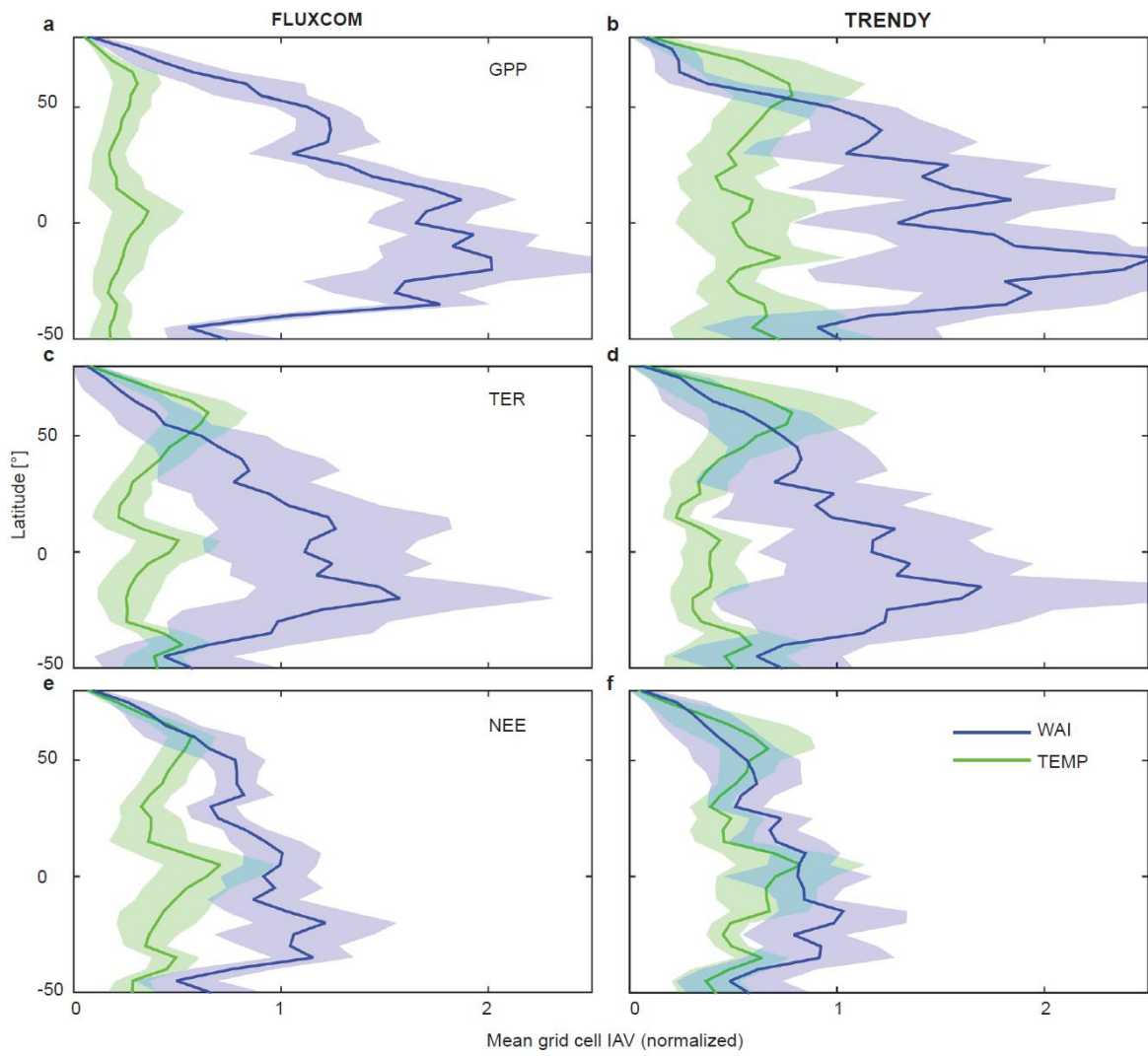
572   Figure 1

573

574

575   Figure 2

576

577

578   Figure 3

579

580

581   Figure 4

a   COV (GPP^{WAI}, TER^{WAI})   b   COR (GPP^{WAI}, TER^{WAI})

c   COV (GPP^{TEMP}, TER^{TEMP})   d   COR (GPP^{TEMP}, TER^{TEMP})

-5   0   5   1   -0.5   0   0.5   1

582